


Article

Failure Analysis of the Crack and Leakage of a Crude Oil Pipeline under CO₂-Steam Flooding

Chengli Song ^{1,*} , Yuanpeng Li ², Fan Wu ², Jinheng Luo ¹, Lifeng Li ¹ and Guangshan Li ¹

¹ State Key Laboratory for Performance and Structure Safety of Petroleum Tubular Goods and Equipment Materials & CNPC Tubular Goods Research Institute, Xi'an 710077, China

² Research Institute of Experiment and Detection of Xinjiang Oil Field Company, CNPC, Karamay 834000, China

* Correspondence: clsong2022@163.com

Abstract: This paper presents the failure analysis of the crack and leakage accident of a crude oil pipeline under CO₂-steam flooding in the western oilfield of China. To analyze the failure behavior and cause, different testing, including nondestructive testing, chemical composition analysis, tensile property testing, metallographic analysis, and microanalysis of fracture and chloride stress corrosion cracking (SCC) testing, are applied in the present study. The obtained results showed that the pipeline under the insulation layer of high humidity, high oxygen content, and high Cl⁻ environment occurred pit corrosion, and the stress concentration area at the bottom of the corrosion pit sprouted cracks. Besides, it is demonstrated that the cracks were much branched, mostly through the crystal, and the fracture showed brittle, which is consistent with the typical characteristics of chloride SCC. Meanwhile, the insufficient Ni content of the pipeline material promoted the process of chloride SCC, and the high-temperature working conditions also aggravated the rate of chloride SCC. In addition, efficient precautions were provided to avoid fracture.

Keywords: crude oil pipeline; 316L stainless steel; CO₂-steam flooding; failure analysis; chloride stress corrosion cracking



Citation: Song, C.; Li, Y.; Wu, F.; Luo, J.; Li, L.; Li, G. Failure Analysis of the Crack and Leakage of a Crude Oil Pipeline under CO₂-Steam Flooding. *Processes* **2023**, *11*, 1567. <https://doi.org/10.3390/pr11051567>

Academic Editor: Iztok Golobič

Received: 3 April 2023

Revised: 4 May 2023

Accepted: 18 May 2023

Published: 21 May 2023



Copyright: © 2023 by the authors. Licensee MDPI, Basel, Switzerland. This article is an open access article distributed under the terms and conditions of the Creative Commons Attribution (CC BY) license (<https://creativecommons.org/licenses/by/4.0/>).

1. Introduction

Dissolving CO₂ gas in crude oil can improve the oil flow ratio and swell the crude oil to achieve the effect of enhanced recovery [1,2]. Moreover, in the global trend of carbon reduction, CO₂ can be effectively buried in this way. Therefore, CO₂ flooding has the economic benefits of recovery enhancement and social benefits of carbon reduction. The application of CO₂ flooding is gradually increasing globally, but it is still in the stage of industrial trials and enhances the application of benefits [3,4]. The literature has so far focused on the study of oil reservoirs applicability assessment, production parameter control and optimization, and miscible effect of CO₂ with crude oil [5–8], with few reported cases of failure of injection and recovery pipelines.

In the western oil field of China, there are many thick oil and super thick oil blocks. To improve recovery, in addition to using CO₂ to reduce the viscosity of the crude oil, steam is also injected to improve oil washing efficiency and wave area again [9–11]. Given the increased corrosion of the recovery media caused by the artificial injection of CO₂ and high-temperature steam, 316L stainless steel is used for the crude oil recovery pipeline to cope with internal corrosion. Moreover, this pipeline lay in the ground and was completely soaked in sanding water underground. The groundwater is mainly recharged by atmospheric precipitation, ground runoff and infiltration and discharged by underground runoff and evaporation. The annual variation of groundwater is about 0.5 m~1.0 m in the region. But, the pipeline is not coated for corrosion protection, except for the external surface, which is covered with an insulation layer.

Nevertheless, the 316L stainless steel pipeline suddenly leaked out after nine months of service. Figure 1 shows the failed pipeline sample after cleaning with water + paraffin. The material of the pipeline is manufactured according to ASTM-A312 [12]. This pipeline sample is $\Phi 168 \text{ mm} \times 5 \text{ mm}$ and 600 mm long. Table 1 presents the design and operating conditions of the pipeline which operating pressure, temperature and flow rate are within allowable limits. In this work, the pipeline's material properties and cracking characteristics will be analyzed by several tests to clarify the causes of leakage failure. And the study results will provide a scientific basis for the selection of materials and corrosion protection of the pipeline under the new conditions of CO₂-steam flooding.



Figure 1. Macroscopic morphology of the pipeline sample.

Table 1. The design and operating conditions of the pipeline.

Medium Type	Design Pressure (MPa)	Operating Pressure (MPa)	Design Temperature (°C)	Operating Temperature (°C)	Allowable Flow Rate (m/s)	Operating Flow Rate (m/s)
Crude oil containing water, associated gas	1.6	0.3	200	98	10	0.4

2. Materials and Methods

2.1. Nondestructive Test

Nondestructive tests can visually detect defects such as cracks and pitting. Given that the material of the failed pipeline is weakly magnetic, as well as large corrosion pits, the penetration testing method is more suitable for the nondestructive testing of this pipeline. To facilitate testing, the pipeline sample was cut into four equal pieces. The external and internal surfaces of the sample are then cleaned with a cleaning agent and sprayed with a uniform layer of white penetrant. After waiting for 10 min, the penetrant is wiped off with a dry cloth, and then the sample surface is wiped with a paper towel soaked with cleaning agent until all the penetrant is wiped off. After the sample has dried naturally in the air, the surface is sprayed with a further layer of red developer. The resulting defect image is then observed and determined.

2.2. Physical and Chemical Performance Test

The chemical composition, mechanical properties and metallographic organization of metal pipes are the most basic physical and chemical properties, which are also the main basis for reflecting the corrosion resistance and strength of pipes. Firstly, an direct reading spectrometer (SPECTRO ARL 4460) was used to analyze the chemical composition of the pipeline body and corrosion pits area. Secondly, three parallel specimens (1#, 2#, 3#) were taken from the pipe's body to test tensile properties by material testing machine (MTS 810), including tensile strength, yield strength and elongation after a fracture. Moreover, the microstructure, grain size and nonmetallic inclusion of the pipeline body and cracks were

analyzed by a metallographic microscope and image analysis system (LEICA MEF4M). The above tests determine whether there are any abnormalities in the material properties of the pipeline.

2.3. Microscopic Characterisation Analysis

This pipeline's corrosion morphology, products and cracking characteristics were characterized to analyze the mechanism of corrosion and cracking. The crack was mechanically opened, and the fracture morphology was analyzed using a scanning electron microscope (TESCAN VEGA 3). The surface products at the cracks were analyzed by an energy spectrum analyzer (XFORD INCA350) and X-ray diffractometer (D8 ADVANCE). In addition, the grains of the metallographic organization of the pipe body was subjected to energy spectroscopy by line scan to characterize whether there were changes in the elements within the grains and at the boundaries. Also, to determine if intergranular corrosion is a possibility. This leads to determining the possibility of intergranular corrosion.

2.4. Corrosion Test

Boiling magnesium chloride SCC standard test can determine the susceptibility of austenitic stainless steel to SCC. According to the standard of ASTM G36, three rectangular specimens (size: 75mm × 15mm × 2mm) were extracted from the pipeline sample. The specimens were bent U-shaped with an indenter with a radius of 8mm. Then the 42% MgCl₂ solution was added to the experimental vessel with a thermometer and condensation tube. The solution will be heated to a constant boiling point of 155 ± 1 °C and then put the specimens into it. And their appearance is monitored periodically at 1h intervals. The susceptibility of the pipeline to chloride SCC is determined by observing whether cracks develop on the surface of the specimens.

3. Results

3.1. Visual Inspection

Figure 2 shows the external wall of the pipeline, which had a large contiguous blackened area. It results from dense corrosion pits in which some oil has been deposited. The depth of these corrosion pits is generally in the range of 1~2mm. Furthermore, corrosion pits and cracks are in the same area. The multiple crack crosses are observed at the bottom of the pits 30~150 mm in length. The main cracks are distributed along the pipeline transversely and longitudinally, as indicated by the arrows in Figure 2. The uncorroded area had a bright metallic luster, and no cracks were found. This suggests that uneven corrosion of the pipeline has occurred.



Figure 2. Macroscopic appearance of cracks and corrosion pits on the external surface (The arrows point to the cracks).

Figure 3 shows that the internal wall of the pipeline possessed multiple cracks at the same location as those on the external wall. Hence, penetration was suspected, but no corrosion pits were observed in the internal wall. Therefore, it should be indicated that the inner wall corrosion of the pipeline is not apparent under the fluid medium and working condition.



Figure 3. Macroscopic appearance of cracks on the internal surface (The arrows point to the cracks).

Figure 4 shows that the cracks originated from the external wall and expanded continuously to the internal wall according to the cross-sectional observation. It is more visualized and proved that the external soil environment of pipeline operation is the main influencing factor of cracking.

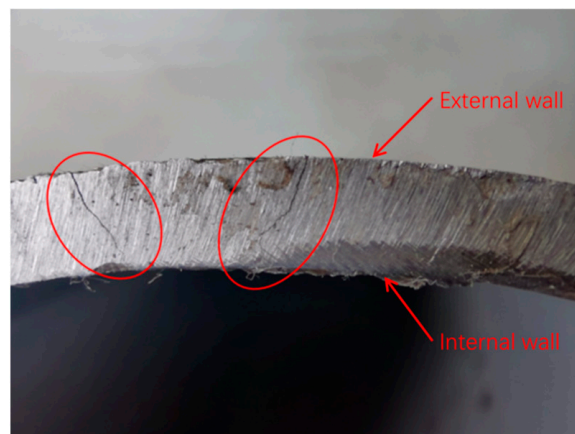


Figure 4. Macroscopic appearance of cracks extension along the section.

3.2. Nondestructive Test

Figure 5 shows the macroscopic morphology of the pipeline after the penetration test. Large defects are observed on the external surface of the pipeline sample, including corrosion pits and cracks. In addition, many obvious branching cracks are observed on the internal surface of the pipeline sample. The cracks on the external wall are concentrated in the corrosion pit area, where the majority are longitudinal, and the cracks are determined as penetrated.



Figure 5. Macroscopic appearance of the pipeline sample after penetration testing: (a) external wall; (b) internal wall.

3.3. Chemical Composition

Table 2 presents the results of the chemical composition analysis of the pipe body and pitting area, in which all elements are within the standard requirements except for the nickel content. The nickel content is lower than the lower limit required by the standard of ASTM-A312, which is an unqualified product. Stainless steel materials are more corrosion resistant because of the addition of the alloy element chromium, molybdenum and nickel. Therefore, a reduction in nickel content will reduce the corrosion resistance of the material [13,14].

Table 2. Results of chemical composition analysis (in wt.%).

Element	C	Si	Mn	P	S	Ni	Cr	Mo	Nb	V	Cu	Al
Pipe body	0.019	0.40	0.91	0.030	0.0017	9.92	16.12	2.03	0.008	0.082	0.25	0.008
Pitting area	0.018	0.40	0.90	0.030	0.0017	9.89	16.14	2.01	0.007	0.083	0.25	0.009
ASTM-A312	≤ 0.035	≤ 1.00	≤ 2.00	≤ 0.045	≤ 0.030	10.00~ 14.00	16.00~ 18.00	2.00~ 3.00	/	/	/	/

3.4. Tensile Property

Table 3 illustrates the obtained results of the tensile properties of the pipe body. The tensile strength, yield strength and elongation after fracture are consistent with the requirements of ASTM-A312 for 316L steel. In addition, it indicates that the pressure-bearing performance of the pipe material without defects can meet the design operating conditions.

Table 3. Tensile characteristics test results.

Sample	Original Gauge Length L_1 (mm)	Final Gauge Length L_2 (mm)	Yield Force F_m (kN)	Maximal Force F_{el} (kN)	Original Cross-Sectional Area S (mm ²)	Tensile Strength R_m (MPa)	Yield Strength R_{el} (MPa)	Elongation after Fracture A (%)
1#	50	81.92	31.92	70.19	128.9	545	248	64
2#	50	81.81	29.40	66.91	121.9	549	241	64
3#	50	81.89	32.07	70.25	128.9	545	249	64
ASTM-A312	/	/	/	/	/	≥485	≥170	≥35

3.5. Metallographic Analysis

Figure 6 shows that the metallographic structure of the pipe body is austenite. No other abnormalities in the metallographic structure of nonmetallic inclusions and grain size. In addition, all cracks in the pipeline sample had similar characteristics, in which they all started from the external wall and extended to the internal wall. The cracks appear to be bifurcated, and no tissue distortion is seen. The main cracks are through crystal cracks, and part of the bifurcation is observed along the crystal fine cracks.

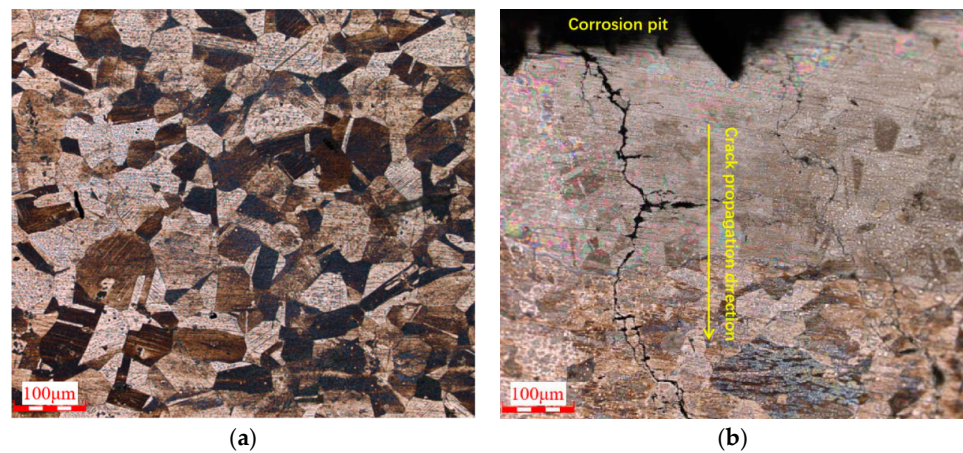


Figure 6. Metallographic structure of the pipeline: (a) pipeline body; (b) crack.

3.6. Microanalysis of Fracture

Figure 7 shows an SEM photo of the fracture at different magnifications. The fracture is flat, without necking, obvious deformation and thinning of wall thickness. As a result, this fracture indicates a clear, brittle fracture. Figure 8 and Table 4 show that the production elements within the cracks have O and Cl from external sources in addition to the metal matrix itself. The physical analysis of the product showed that it is mainly Fe_2O_3 which stems from oxygen corrosion, as shown in Figure 9.

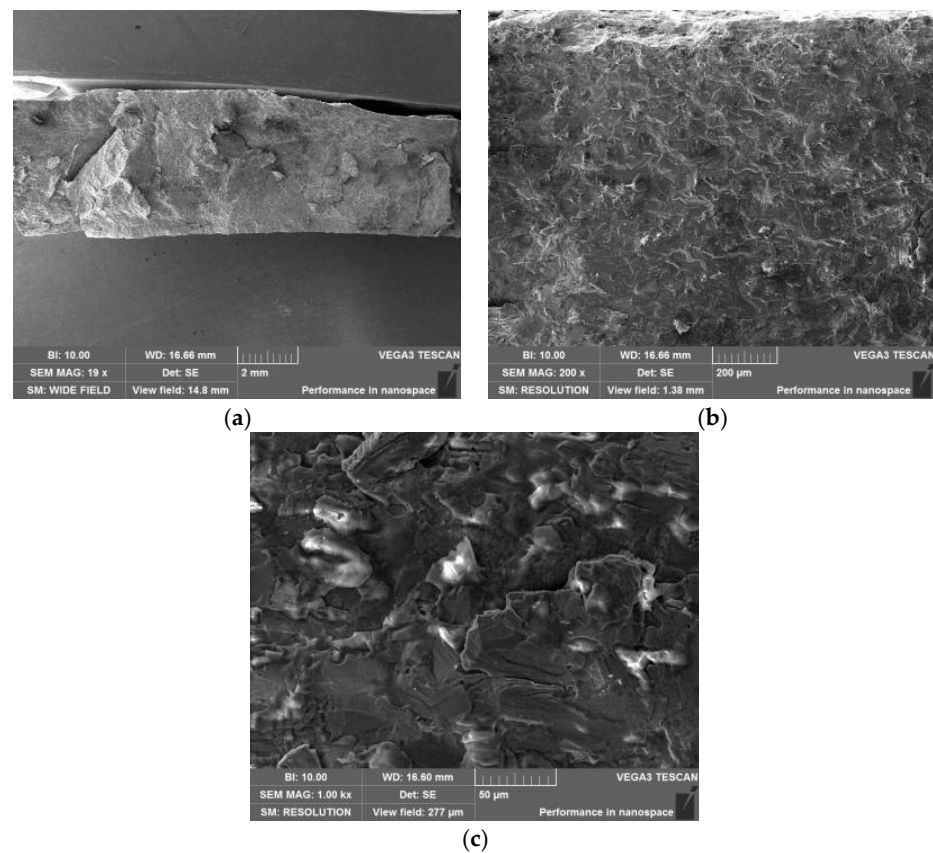
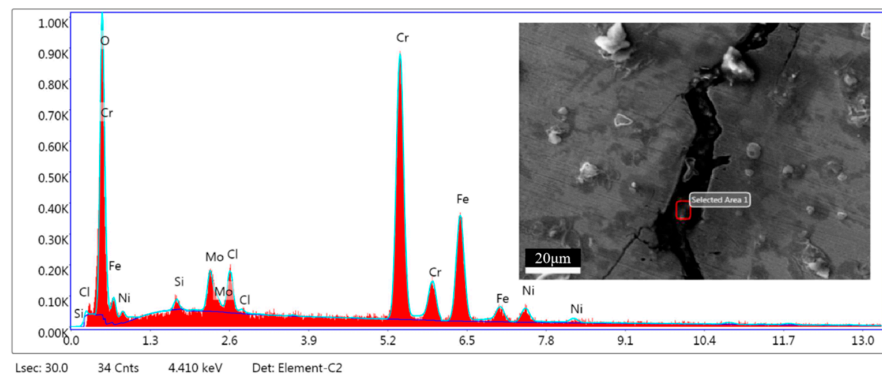
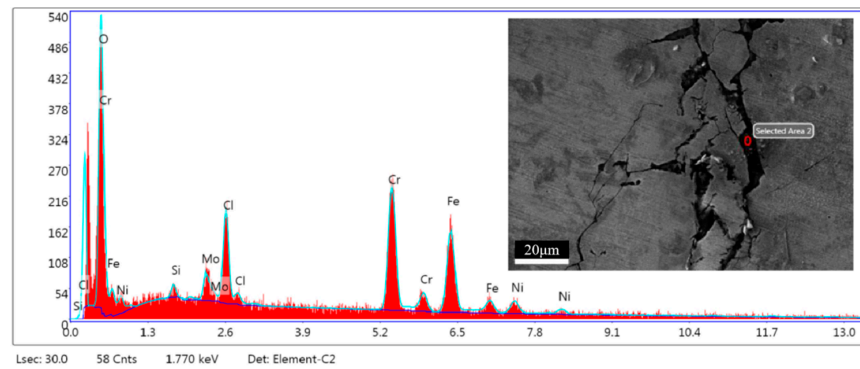


Figure 7. Micromorphology of the fracture: (a) 19 \times ; (b) 200 \times ; (c) 1000 \times .



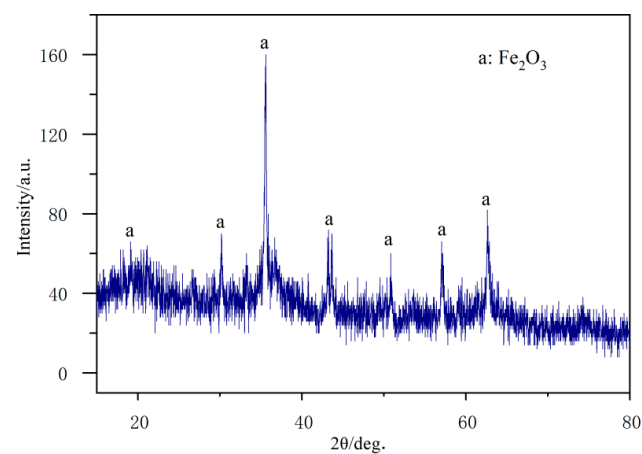
(a)



(b)

Figure 8. Micromorphology and EDS analysis result of the cracks: (a) Area 1; (b) Area 2.**Table 4.** Elemental content based on EDS analysis.

Elements	Area 1		Area 2	
	In wt.%	In at.%	In wt.%	In at.%
O	17.14	40.99	23.26	49.37
Si	0.70	0.95	1.33	1.60
Mo	5.21	2.08	5.02	1.78
Cl	3.04	3.28	9.47	9.07
Cr	43.75	32.19	28.47	18.60
Fe	25.82	17.69	27.11	16.49
Ni	4.34	2.83	5.34	3.09

**Figure 9.** XRD patterns of the corrosion products.

Besides, Figure 10 shows the content of each element has no significant change along grain boundaries. Therefore, it shows no carbide precipitation at the grain boundary, excluding the possibility of intergranular corrosion.

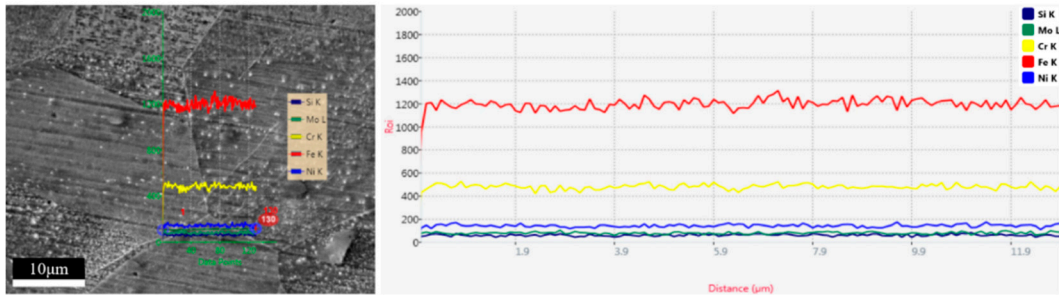


Figure 10. Linear EDS analysis along grain boundaries.

3.7. Chloride SCC Test

After 20 h of the chloride SCC test, cracks appear on the surface of specimens (1#, 2# and 3#), as shown in Figure 11. And the cracks are mainly concentrated in the bending section of the specimen, with fewer cracks in the straight edge section, as shown in Figure 12.

To further analyze the crack morphology, specimen 1# is separated along the longest crack in the center. Figure 13a presents the upper part of the fracture is corroded, indicating that the cracking starts from the outer wall and gradually extends to the interior. Figure 13b shows a tearing ling-like quasi-dissociative fracture, which was typical fracture morphology of crystal penetration.

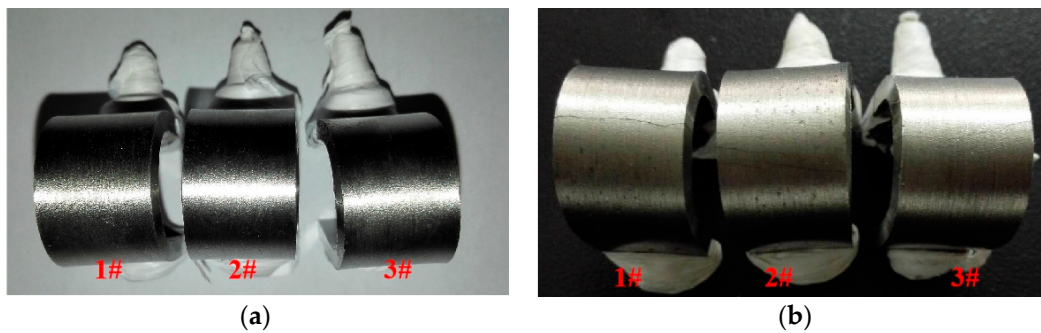


Figure 11. Chloride SCC test results: (a) before the test; (b) after the test.

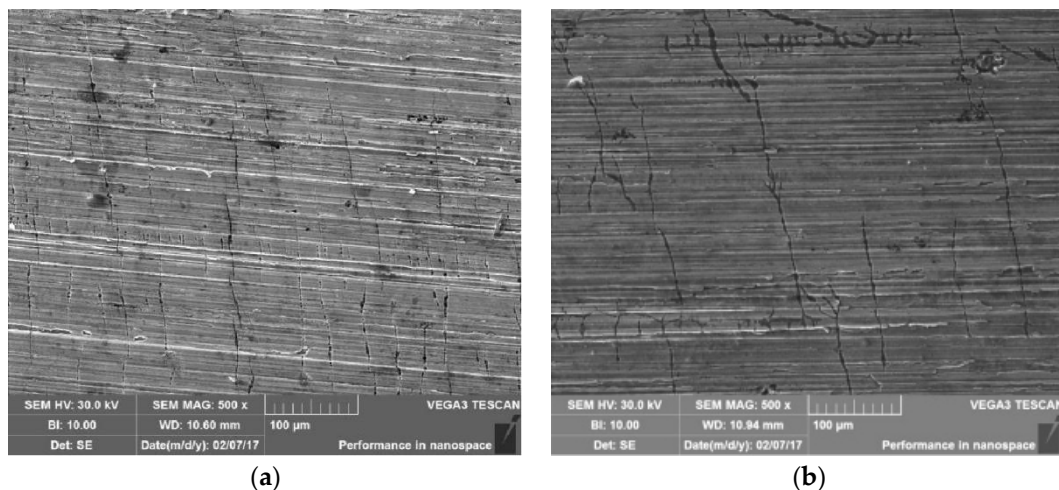


Figure 12. Crack morphology: (a) bending section; (b) straight edge.

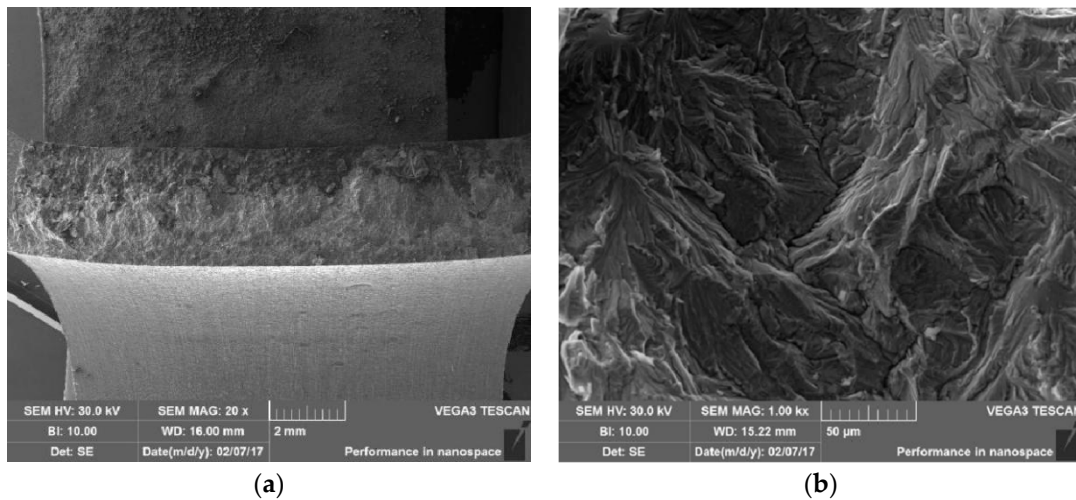


Figure 13. Fracture morphology of specimen 1#: (a) 20 \times ; (b)1000 \times .

4. Discussion

The failure type of the pipeline is cracking, with the cracks starting from the bottom of the corrosion pit on the external wall and extending to the internal wall. Moreover, the branching of the cracks, which are mainly crystalline, and the fracture show brittle characteristics. Coupled with the fact that the pipe material is 316L austenitic stainless steel, it is judged that the failure of the pipeline is consistent with the significant characteristics of chloride SCC. SSC is a localized corrosion damage in metal materials under the combined action of tensile stress and corrosive media. The following three specific analyses regarding environment, stress and material will be carried out.

4.1. Corrosion Environment Analysis

It uses a cyclic injection process of CO₂ and steam in the oilfield, resulting in a high recovery pipeline temperature of 98 °C. The API RP 571 standard describes the starting temperature at which chloride SCC occurs as 60 °C [15]. The API RP 581 standard states chloride cracking must be considered for environments above 38 °C under severe conditions [16]. Therefore, the operating temperature of the pipeline is sensitive to chloride SCC.

Macroscopic inspection reveals the existence of dense corrosion pits on the external wall of the pipeline, and XRD analysis further verifies the presence of Fe₂O₃, which is mainly a product of oxygen corrosion [17,18]. This is mainly because groundwater often contains dissolved oxygen from the air. Furthermore, it indicates that the insulation layer had broken down. Hence, localised pipeline corrosion is caused by underground water penetration into the insulation. Moreover, the higher the temperature, the more serious the corrosion will be, eventually resulting in large areas of pitting pits on the external wall of the pipeline.

In addition, underground water in the western region of China usually contains more Cl ions (200~1000 mg/L), constituting the basic condition for chloride SCC. At higher temperatures, the evaporation of water from the metal surface leads to a constant concentration and deposition of Cl ions. This will cause localised rupture of the stainless-steel passivation film. The formation of passivation-activation microcells at metal surfaces with and without passivation films will accelerate anodic dissolution and produce anodic polarisation [19–21]. As the corrosion pits deepen, small anodes and large cathodes will appear inside and outside, resulting in ever larger corrosion pits [22–24].

Moreover, it has been shown that the susceptibility to chloride SCC is significantly increased in the presence of both Cl ions and dissolved oxygen [25–27]. This is because the rate of oxygen consumption in the crack is greater than the rate of diffusion, leaving the crack tip still in a low oxygen state [28,29]. A corrosion potential gradient drives anions (e.g., chloride, sulphate, and hydroxide ions) deeper into the crack, while cations (hydrogen,

sodium, and zinc ions) move outwards from the crack. This, in turn, causes the chloride ions to accumulate rapidly at the crack tip, creating very high concentrations. As a result, Cl^- ions destroy the passivation film more quickly and further reduce the rate of passivation film formation [30,31]. The aggressive Cl^- ions invaded the grain in multi-directions promoted by dislocation motion, facilitating the main crack to bifurcate [32].

4.2. Stress Analysis

Corrosion pits have formed after significant localised corrosion has occurred on the external wall of this pipeline. Under operating pressure, soil pressure and other residual stress, there is a large stress concentration at the bottom of the corrosion pits. Residual stresses account for the largest proportion of several stresses because the pipeline is subjected to various processes, such as cooling, thermal processing, welding, etc., which can cause residual stresses. Besides, 316L austenitic stainless steel also has process hardening characteristics. The presence of stress makes the passivation film surface in the stress concentration area enriched with more chloride ions, which reduces the thickness, integrity of the passivation film, and pitting resistance [33,34]. This results in faster anodic dissolution in the stress concentration zone. In the low-stress area, the concentration of chloride ions is relatively low, and the passivation film thickness is greater and more complete, resulting in greater resistance to pitting corrosion. Figure 14 shows the model for stress corrosion of stainless steel.

The stress concentration area is prone to cracking [35,36], and the cracks in this pipeline all start at the bottom of the corrosion pits. As a result, once a crack has developed, the passivation film formed at the crack's tip differs from that away from the crack [37]. It is much looser and less stable, leading to cracking of the passivation film. The corrosion rate at the tip of the crack will be higher than at other locations [37], thus allowing the crack to expand in a direction perpendicular to the stress. Once the formation of micro cracks, its expansion rate is much faster than other types of localized corrosion, so SCC is the most destructive and damaging type of corrosion among all types of corrosion.

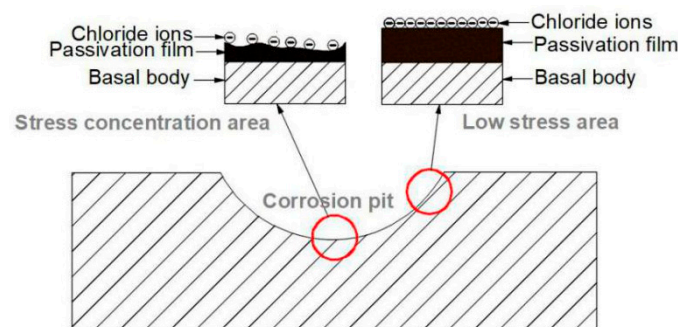


Figure 14. Mechanism model of chloride SCC.

4.3. Material Analysis

The composition of alloy materials, organizational structure, and heat treatment will also affect its SCC resistance. For example, austenitic stainless steel is generally considered susceptible to chloride SCC. In contrast, ferritic stainless steel and duplex stainless steel have better resistance to chloride SCC performance when exposed to Cl^- environments for long periods. This pipeline insulation layer broke down, resulting in groundwater containing Cl^- ions and dissolved oxygen seeping into the insulation. Thus, the environment of high temperature, high humidity, and high Cl^- under the insulation provides favourable conditions for chloride SCC for 316L material.

In addition, Ni is the only important element to improve the stress corrosion resistance of austenitic stainless steel [38,39]. The standard API RP 571 also proposes that the Ni content of the alloy material is the most sensitive to chloride SCC at 8~12% [15], while the chemical composition analysis of the pipeline has a Ni content of about 9.9%, which is in

the sensitive range of chloride SCC. At the same time, an EDS line scan of the pipeline grain structure revealed no significant change in alloying element content, ruling out intergranular corrosion cracking due to intergranular Cr depletion.

The accelerated test for chloride SCC confirmed that the pipeline cracked after 20 h of testing, and it can be concluded that the pipeline does have a high susceptibility to chloride SCC.

Based on the above analysis, it can be seen that the pipeline leakage failure process is divided into three stages. In the first stage, due to the presence of groundwater containing dissolved oxygen and Cl ions, the corrosion process was localized. Under the action of high temperature (98 °C), the local corrosion intensifies continuously. In the second stage, many cracks were generated at the bottom of the corrosion pits. In the third stage, due to the local concentration of stress and the continuous action of corrosion, the crack grew rapidly and led to the final failure of the material.

5. Methods for Chloride SCC Control of Stainless Steel

Three factors are required for SCC to occur: material, environment and stress. If any of these factors can be controlled, then it is possible to prevent or avoid the occurrence of chloride SCC in stainless steel.

Firstly, according to the specific environment in which the material is used, avoid using materials sensitive to chloride SCC. In general, in hot water and high-temperature water conditions, high chromium ferritic stainless steel, ferritic-austenitic duplex stainless steel, ultra-low carbon stainless steel and high nickel stainless steel can be considered to choose. However, in both, the need to resist SCC and require higher strength, ferritic-austenitic duplex stainless steel is more appropriate. On the other hand, in high concentrations of chloride media, ferritic stainless steel with low carbon and high chromium can be used, and high silicon chromium-nickel stainless steel is also a better choice.

Secondly, isolating the material from the corrosive environment is the most effective way to avoid SCC, such as using coatings or corrosion inhibitors. Reducing the concentration of Cl ions and operating temperature in the environment and preventing Cl ions adsorption and concentration are also the ways to slow down SCC. In addition, the mass fraction of oxygen should be reduced to a lower value when stainless steel is used to dissolve oxygen chloride.

Thirdly, measures should be taken during pipeline manufacturing to eliminate or reduce the residual stress in processing and welding. Surface treatment methods (such as shot peening, surface heat treatment, etc.) can also be used to reduce the residual compressive stress on the surface. Stress removal or elimination can also be performed using hydrostatic tests, temperature difference tensile and vibration.

6. Conclusions and Recommendations

- (1) The pipeline experienced localized external corrosion in groundwater containing dissolved oxygen and Cl ions, and leakage failure occurred due to chloride SCC in the stress concentration area at the bottom of the corrosion pits.
- (2) The Ni content of the pipeline material was lower than the standard product requirements and within the sensitive content range of chloride SCC, which accelerated the cracking of the pipeline. As well as the high temperature of the recovered medium under CO₂ and steam combined flooding promoted the progress of chloride SCC.
- (3) Several Specific and practical recommendations are then proposed from both manufacturing and maintenance points of view. First, replacing the pipeline with 2205 duplex stainless steel pipe is feasible. Second, by reducing the operating temperature of the pipeline, the development of SCC will be slowed. Third, the buried pipelines should adopt an anticorrosion layer + cathodic protection to slow the occurrence of external corrosion damage under the new process of CO₂-steam combined flooding. Fourth, similar pipelines need to be excavated for defect inspection and safety evaluation,

and the severely corroded external pipeline section needs to repair by B-type sleeve, carbon fiber (or glass fiber) reinforcement, etc.

Author Contributions: Methodology, C.S.; Data curation, Y.L. and F.W.; Writing—original draft J.L. and L.L.; Writing review & editing, G.L. All authors have read and agreed to the published version of the manuscript.

Funding: This research was funded by Shaanxi Province Innovation Capacity Support Program Project (2023KJXX—091) and CNPC research found (2020D-5008).

Institutional Review Board Statement: Not applicable.

Informed Consent Statement: Not applicable.

Data Availability Statement: Not applicable.

Conflicts of Interest: The authors declare no conflict of interest.

References

1. Yao, J.; Han, H.; Yang, Y.; Song, Y.; Li, G. A review of recent progress of carbon capture, utilization, and storage (CCUS) in China. *Appl. Sci.* **2023**, *13*, 1169. [\[CrossRef\]](#)
2. Zhou, X.; Yuan, Q.; Peng, X.; Zeng, F.; Zhang, L. A critical review of the CO₂ huff ‘n’ puff process for enhanced heavy oil recovery. *Fuel* **2018**, *215*, 813–824. [\[CrossRef\]](#)
3. J Luo, S.; Hou, Z.M.; Feng, G.Q.; Liao, J.X.; Haris, M.; Xiong, Y. Effect of reservoir heterogeneity on CO₂ flooding in tight oil reservoirs. *Energies* **2022**, *15*, 3015–3022.
4. Jiang, K.; Ashworth, P.; Zhang, S.; Liang, X.; Angus, D. China’s carbon capture, utilization and storage (CCUS) policy: A critical review. *Renew. Sustain. Energy Rev.* **2019**, *119*, 109601. [\[CrossRef\]](#)
5. Makarova, A.A.; Mantorova, I.V.; Kovalev, D.A.; Kutovoy, I.N. The modeling of mineral water fields data structure. In Proceedings of the 2021 IEEE Conference of Russian Young Researchers in Electrical and Electronic Engineering (ElConRus), Moscow, Russia, 26–29 January 2021; pp. 517–521.
6. Makarova, A.A.; Kaliberda, I.V.; Kovalev, D.A.; Pershin, I.M. Modeling a production well flow control system using the example of the Verkhneberezhovskaya area. In Proceedings of the 2022 Conference of Russian Young Researchers in Electrical and Electronic Engineering (ElConRus), Saint Petersburg, Russia, 25–28 January 2022; pp. 760–764.
7. Wang, T.; Wang, L.; Meng, X.; Chen, Y.; Song, W.; Yuan, C. Key parameters and dominant EOR mechanism of CO₂ miscible flooding applied in low-permeability oil reservoirs. *Geoenergy Sci. Eng.* **2023**, *225*, 211724. [\[CrossRef\]](#)
8. Morgan, A.; Ampomah, W.; Grigg, R.; Dai, Z.; You, J.; Wang, S. Techno-economic life cycle assessment of CO₂-EOR operations towards net negative emissions at Farnsworth field unit. *Fuel* **2023**, *342*, 127897. [\[CrossRef\]](#)
9. Heidari, P.; Kordestany, A.; Sepahvand, A. An experimental evaluation of oil recovery by steam alternative CO₂ injection in naturally fractured reservoirs. *Energy Sources* **2013**, *35*, 1498–1507. [\[CrossRef\]](#)
10. Yuan, R.; Yang, Z.D.; Guo, B.; Wang, X.W.; Zhang, L.Q.; Lin, R.Y. Potential analysis of enhanced oil recovery by superheated steam during steam-assisted gravity drainage. *Energy Technol. Gener. Conversion. Storage Distrib.* **2021**, *9*, 2100135. [\[CrossRef\]](#)
11. Liu, W.; Du, L.; Zou, X.; Liu, T.; Wu, X.; Wang, Y.; Dong, J. Experimental study on the enhanced ultra-heavy oil recovery using an oil-soluble viscosity reducer and CO₂ assisted steam flooding. *Geoenergy Sci. Eng.* **2023**, *222*, 211409. [\[CrossRef\]](#)
12. ASTM-A312-2018; Standard specification for seamless, welded, and heavily cold-worked austenitic stainless steel pipes. ASTM: West Conshohocken, PA, USA, 2018.
13. Yu, H.; Luo, Z.; Zhang, X.; Feng, Y.; Xie, G. A comparative study of the microstructure and corrosion resistance of Fe-based/B4C composite coatings with Ni-added or Cu-added by vacuum cladding. *Mater. Lett.* **2023**, *335*, 133730. [\[CrossRef\]](#)
14. Zhang, S.; Bian, T.; Mou, L.; Yan, X.; Zhang, J.; Zhang, Y.; Liu, B. Alloy design employing Ni and Mo low alloying for 3Cr steel with enhanced corrosion resistance in CO₂ environments. *J. Mater. Res. Technol.* **2023**, *24*, 1304–1321. [\[CrossRef\]](#)
15. API RP 571-2020; Damage Mechanisms Affecting Fixed Equipment in the Refining Industry. API: Minnesota City, MN, USA, 2020.
16. API RP 581-2016; Risk-based inspection methodology. API: Minnesota City, MN, USA, 2016.
17. Luo, B.W.; Zhou, J.; Bai, P.P.; Zheng, S.Q.; An, T.; Wen, X.L. Comparative study on the corrosion behavior of X52, 3Cr, and 13Cr steel in an O₂-H₂O-CO₂ system: Products, reaction kinetics, and pitting sensitivity. *Int. J. Miner. Metall. Mater.* **2017**, *24*, 646–656. [\[CrossRef\]](#)
18. Song, C.L.; Liu, X.B.; Pan, X. Failure analysis of the leakage and ignition of an oil-gas mixture transportation pipeline. *J. Fail. Anal. Preven.* **2022**, *22*, 259–266. [\[CrossRef\]](#)
19. Zhang, S.H.; Hou, L.F.; Wei, Y.H.; Du, H.Y.; Wei, H.; Liu, B.S.; Chen, X.B. Dual functions of chloride ions on corrosion behavior of mild steel in CO₂ saturated aqueous solutions. *Mater. Corros.* **2019**, *70*, 888–896. [\[CrossRef\]](#)
20. Wang, Z.; Liu, Z.-X.; Jin, J.; Tang, D.-Z.; Zhang, L. Selective corrosion mechanism of CoCrFeMoNi high-entropy alloy in the transpassive region based on the passive film characterization by ToF-SIMS. *Corros. Sci.* **2023**, *218*, 111206. [\[CrossRef\]](#)

21. Cui, Y.-W.; Chen, L.-Y.; Chu, Y.-H.; Zhang, L.; Li, R.; Lu, S.; Wang, L.; Zhang, L.-C. Metastable pitting corrosion behavior and characteristics of passive film of laser powder bed fusion produced Ti-6Al-4V in NaCl solutions with different concentrations. *Corros. Sci.* **2023**, *215*, 111017. [[CrossRef](#)]
22. Cong, S.; Tong, K.; Li, D.F.; Chen, Z.X.; Cai, K. Leakage failure analysis of the ERW steel pipeline. *Mater. Sci. Forum* **2020**, *993*, 1224–1229. [[CrossRef](#)]
23. Hua, Y.; Shamsa, A.; Barker, R.; Neville, A. Protectiveness, morphology and composition of corrosion products formed on carbon steel in the presence of Cl^- , Ca^{2+} and Mg^{2+} in high-pressure CO_2 environments. *Appl. Surf. Sci.* **2018**, *455*, 667–682. [[CrossRef](#)]
24. Zhang, B.; Ma, X.L. A review—Pitting corrosion initiation investigated by TEM. *J. Mater. Sci. Technol.* **2019**, *35*, 1455–1465. [[CrossRef](#)]
25. Congleton, J.; Shih, H.C.; Shoji, T.; Parkins, R.N. The stress corrosion cracking of type 316 stainless steel in oxygenated and chlorinated high-temperature water. *Corros. Sci.* **1985**, *25*, 769–788. [[CrossRef](#)]
26. Andresen, P.L.; Morra, M.M. IGSCC of non-sensitized stainless steels in high-temperature water. *J. Nucl. Mater.* **2008**, *383*, 97–111. [[CrossRef](#)]
27. Du, D.H.; Chen, K.; Lu, H.; Zhang, L.F.; Shi, X.Q.; Xu, X.L.; Andresen, P.L. Effects of chloride and oxygen on stress corrosion cracking of cold worked 316/316L austenitic stainless steel in high-temperature water. *Corros. Sci.* **2016**, *110*, 134–142. [[CrossRef](#)]
28. Andresen, P.L.; Young, L.M. *Characterization of the Roles of Electrochemistry, Convection and Crack Chemistry in Stress Corrosion Cracking*; No. CONF-950816-; NACE International: Houston, TX, USA, 1995; pp. 579–596.
29. Congleton, J.; Shoji, T.; Parkins, R.N. The stress corrosion cracking of reactor pressure vessel steel in high-temperature water. *Corros. Sci.* **1985**, *25*, 633–650. [[CrossRef](#)]
30. Xu, L.; Wu, P.; Zhu, X.; Zhao, G.; Ren, X.; Wei, Q.; Xie, L. Structural characteristics and chloride intrusion mechanism of the passive film. *Corros. Sci.* **2022**, *207*, 110563. [[CrossRef](#)]
31. Ibrahim, M.A.M.; Rehim, S.S.A.E.; Hamza, M.M. Corrosion behavior of some austenitic stainless steels in chloride environments. *Mater. Chem. Phys.* **2009**, *115*, 80–85. [[CrossRef](#)]
32. Chu, T.; Shao, C.; Wang, Y.; Ma, N.; Lu, F. Crack branching behavior and amorphous film formation mechanism during SCC expanding test for multi-layers weld metal of NiCrMoV steels. *Mater. Des.* **2022**, *216*, 110520. [[CrossRef](#)]
33. Hou, Q.; Liu, Z.Y.; Li, C.T.; Li, X.G.; Shao, J.M. Degradation of the oxide film formed on Alloy 690TT in a high-temperature chloride solution. *Appl. Surf. Sci.* **2019**, *467*, 1104–1112. [[CrossRef](#)]
34. Song, Z.; Zhang, Y.; Liu, L.; Pu, Q.; Jiang, L.; Chu, H.; Luo, Y.; Liu, Q.; Cai, H. Use of XPS for quantitative evaluation of tensile-stress-induced degradation of passive film on carbon steel in simulated concrete pore solution. *Constr. Build. Mater.* **2021**, *274*, 121779. [[CrossRef](#)]
35. Wenman, M.R.; Trethewey, K.R.; Jarman, S.E.; Chard-Tuckey, P.R. A finite-element computational model of chloride-induced transgranular stress-corrosion cracking of austenitic stainless steel. *Acta Mater.* **2008**, *56*, 4125–4136. [[CrossRef](#)]
36. Beber, V.C.; Schneider, B. Fatigue of structural adhesives under stress concentrations: Notch effect on fatigue strength, crack initiation and damage evolution. *Int. J. Fatigue* **2020**, *140*, 105824. [[CrossRef](#)]
37. Zhang, G.A.; Cheng, Y.F. Micro-electrochemical characterization of corrosion of pre-cracked X70 pipeline steel in a concentrated carbonate/bicarbonate solution. *Corros. Sci.* **2010**, *52*, 960–968. [[CrossRef](#)]
38. Yazdanpanah, A.; Pezzato, L.; Dabalà, M. Stress corrosion cracking of AISI 304 under chromium variation within the standard limits: Failure analysis implementing microcapillary method. *Eng. Fail. Anal.* **2022**, *142*, 106797. [[CrossRef](#)]
39. Das, N.K.; Suzuki, K.; Ogawa, K.; Shoji, T. Early stage SCC initiation analysis of fcc Fe-Cr-Ni ternary alloy at 288 °C: A quantum chemical molecular dynamics approach. *Corros. Sci.* **2009**, *51*, 908–913. [[CrossRef](#)]

Disclaimer/Publisher’s Note: The statements, opinions and data contained in all publications are solely those of the individual author(s) and contributor(s) and not of MDPI and/or the editor(s). MDPI and/or the editor(s) disclaim responsibility for any injury to people or property resulting from any ideas, methods, instructions or products referred to in the content.